

Accuracy of downfolding based on the constrained random phase approximation

Hiroshi Shinaoka,¹ Rei Sakuma,² Matthias Troyer,¹ and Philipp Werner³

¹*Theoretische Physik, ETH Zürich, 8093 Zürich, Switzerland*

²*Department of Physics, Division of Mathematical Physics,*

Lund University, Sölvegatan 14A, 223 62 Lund, Sweden

³*Department of Physics, University of Fribourg, 1700 Fribourg, Switzerland*

(Dated: June 17, 2022)

We study the reliability of the constrained random phase approximation (cRPA) method for the calculation of low-energy effective Hamiltonians by considering multi-orbital lattice models with one strongly correlated “target” band and several weakly correlated “screening” bands. The full multi-orbital system is solved within dynamical mean field theory (DMFT), while the effective low-energy models with retarded and off-site interactions are treated within the extended dynamical mean field (EDMFT) framework. By comparing the quasi-particle weights for the correlated bands, we determine the parameter regime in which the effective model provides a good description of the low-energy properties of the multi-band system.

PACS numbers: 71.20.-b,71.27.+a,71.30.+h

I. INTRODUCTION

Strongly correlated electron systems attract much attention because they exhibit remarkable many-body phenomena. Establishing a first-principles theoretical framework for describing the electronic properties of this class of materials is a great challenge. Methods based on density functional theory (DFT)^{1,2} have been successfully used to understand and predict the properties of weakly correlated materials such as elemental metals. Although the DFT formalism is exact in principle, the density functionals used in calculations are approximate, e.g., based on the local density approximation (LDA),² because the exact form of the functional is unknown. The result is a static mean-field description of the electronic structure. Applying this approach to strongly correlated materials misses fundamental aspects, such as quantum fluctuations and Mott physics.

On the other hand, a variety of sophisticated numerical methods have been developed to treat effective models of strongly correlated electrons in lattice systems such as the Hubbard model. Examples include quantum Monte Carlo methods,³ dynamical mean-field theory (DMFT),⁴ the variational Monte Carlo method,⁵ density matrix renormalization group⁶, and tensor network methods. These methods take into account correlation effects beyond the static mean-field level. However, they cannot be directly applied to real materials, which are typically characterized by a complex and hierarchical electronic structure. In most transition metal oxides, there are only a few correlated bands near the Fermi level, which are typically of d character, and in the simplest situation these bands are well separated in energy from the higher- and lower-lying bands (which we will collectively denote as “high-energy bands”). Although high-energy bands are usually less correlated, they can substantially affect the low-energy electrons through the screening of the Coulomb interaction. Thus, we cannot simply neglect the high-energy degrees of freedom in realistic cal-

culations. A similar structure is found also in lanthanide or actinide oxides and organic compounds.

In recent years much effort has been devoted to establishing reliable first-principles methods for strongly correlated materials which exploit this hierarchical structure.⁷ The strategy is to construct an effective low-energy lattice model, which contains only a few degrees of freedom, by eliminating the high-energy degrees of freedom in a systematic manner. In practice, we compute effective Coulomb interactions in the low-energy model by taking into account the screening effects by the high-energy bands using a first-principles calculation based on DFT. Then, this strongly correlated effective model is solved accurately by quantum Monte Carlo methods or DMFT. The procedure which leads to the low-energy effective model is called downfolding. One widely used method for computing screening effects is the constrained random approximation (cRPA) method.⁸ It has been applied to a variety of transition metal oxides^{9–12} and organic compounds^{13–16} to investigate metal-insulator transitions, magnetism, and superconductivity.

While the logic behind the cRPA method is compelling, it is at the present stage a recipe, whose accuracy and limitations have not been established. To the best of our knowledge, no systematic effort has yet been made to clarify under which circumstances and to what extent cRPA is reliable. An obvious difficulty is that an accurate numerical solution of the original multi-band problem is in general not possible. For this reason we address the issue in a simple model context where the accuracy of the cRPA downfolding scheme can be tested systematically. We consider multi-orbital Hubbard models in three dimensions and derive effective low-energy models by the cRPA downfolding scheme. Then, we solve both the full model and the effective model using a DMFT or extended DMFT approximation. By comparing quantities such as mass enhancements, we can determine the parameter regions in which the effective model provides an accurate description of the low-energy properties of the original

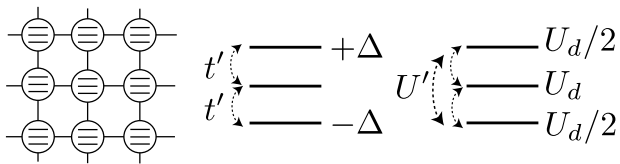


FIG. 1: Three-orbital model on a cubic lattice. The three levels are split by orbital dependent on-site energies. We include an orbital-offdiagonal transfer t' , but the highest and lowest orbitals are not connected by a hopping term. The onsite repulsion for the target orbital is denoted by U_d , while the highest and lowest orbitals are less correlated with an on-site repulsion of $U_d/2$. The inter-orbital repulsion U' acts between all pairs of orbitals.

multi-band model.

The rest of this paper is organized as follows. In Sec. II, we introduce the model used in this study. In Sec. III, we explain the cRPA downfolding procedure. Section IV describes the details of the DMFT calculations. We discuss results of the downfolding and DMFT calculations in Sec. V. Section VI contains the conclusions and a brief outlook.

II. MODEL

To test the accuracy of downfolding, we consider an N_{orb} -orbital Hubbard model on a cubic lattice with orbital-diagonal transfer $t = 1$ between nearest-neighbor sites. Its Hamiltonian is given by

$$\begin{aligned} \mathcal{H} = & - \sum_{\langle i,j \rangle} \sum_{\alpha\sigma} \hat{c}_{i\alpha\sigma}^\dagger \hat{c}_{j\alpha\sigma} + \sum_i \sum_{\alpha} (E_{\alpha} - \mu) \hat{n}_{i\alpha} \\ & - t' \sum_i \sum_{\sigma} \sum_{\alpha=\alpha_{\text{target}}, \beta \neq \alpha} \left(\hat{c}_{i\alpha\sigma}^\dagger \hat{c}_{i\beta\sigma} + \hat{c}_{i\beta\sigma}^\dagger \hat{c}_{i\alpha\sigma} \right) \\ & + \sum_{i\alpha} U_{\alpha} \hat{n}_{i\alpha\uparrow} \hat{n}_{i\alpha\downarrow} + \sum_i \sum_{\alpha < \beta} U' \hat{n}_{i\alpha} \hat{n}_{i\beta}, \end{aligned} \quad (1)$$

where i and j are site indices, while α and β are orbital indices. The energies E_{α} are orbital-dependent potentials given by $E_{\alpha} = -\Delta$ for $\alpha = 1, \dots, \alpha_{\text{target}} - 1$, $E_{\alpha} = 0$ for $\alpha = \alpha_{\text{target}}$, and $E_{\alpha} = \Delta$ for $\alpha = \alpha_{\text{target}} + 1, \dots, N_{\text{target}}$. Here, $\alpha_{\text{target}} = (N_{\text{orb}} - 1)/2$ is the index of the orbital corresponding to the target band and $\Delta > 0$ (see illustration for $N_{\text{orb}} = 3$ in Fig. 1). We consider only density-density interactions. The onsite repulsion U_{α} is taken to be $U_{\alpha} = U_d (> 0)$ for the target orbital and $U_{\alpha} = U_d/2 (> 0)$ for the high-energy orbitals because screening bands are usually less correlated than target bands in real materials. We also include inter-orbital interactions U' . We adjust the chemical potential μ in the DMFT self-consistent procedure such that the number of electrons is N_{orb} (half filling).

We show the band structure of a three-orbital model for $\Delta = 7$ and $t' = 2$ in Fig. 2(a). The half-filled target band is sandwiched between two high-energy bands.

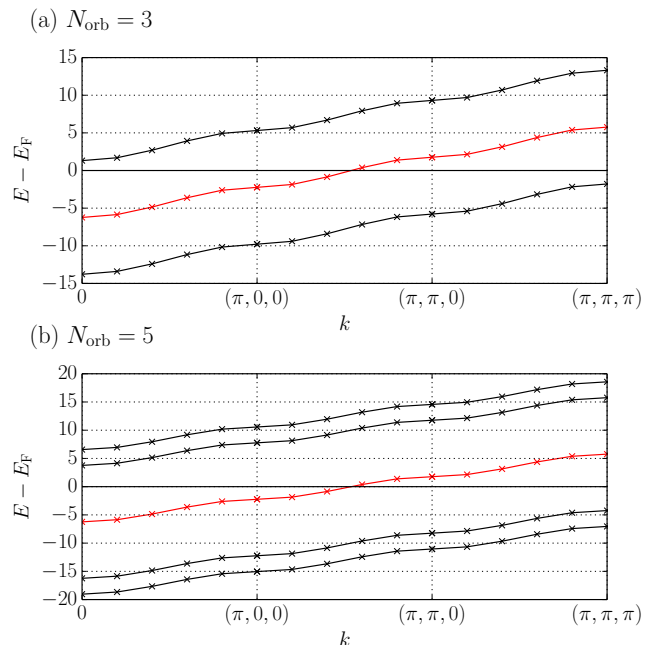


FIG. 2: (Color online) Band structures of (a) the three-orbital model for $\Delta = 7$ and $t' = 2$ and (b) the five-orbital model for $\Delta = 10$ and $t' = 4$. The half-filled target bands are shown in red.

Although the target band and the screening bands are separated by a direct gap at each k point, the indirect gap is negative.

For the five-orbital model, we take $\Delta = 10$ and $t' = 4$. The corresponding band structure is shown in Fig. 2(b). In this model, the interorbital hopping t' splits the screening bands on both sides of the Fermi energy. To keep the screening bands away from the Fermi level, we need a sufficiently large Δ .

Although both band structures are particle-hole symmetric, the interactions break the particle-hole symmetry.

Another notable issue is the existence of a physical lower bound for U'/U_d . Let us consider the following two electronic configurations in the atomic limit. The first one corresponds to the situation which we assume in the downfolding discussion: The lower screening bands are fully occupied, while the upper screening bands are empty and the target band is half-filled. The second configuration is the state where all bands are half-filled. The energy difference between the first and the second state is given by

$$- \frac{N_{\text{orb}} - 1}{2} \left(U' - \frac{U_d}{4} + 2\Delta \right). \quad (2)$$

(assuming paramagnetic solutions). We immediately see that the first state is unstable to charge redistribution when $U'/U_d < 0.25$ and $U_d, U' \gg \Delta$. Thus, in the present study, we restrict ourselves to the regime $U'/U_d \geq 0.25$.

III. CONSTRAINED RANDOM PHASE APPROXIMATION (CRPA)

We start by considering the Hamiltonian

$$\mathcal{H} = H^0 + V, \quad (3)$$

$$H^0 = \sum_{n=1}^N h^0(r_n) = \sum_{n=1}^N \left[-\frac{1}{2} \nabla_n^2 + V_{\text{ext}}(r_n) \right], \quad (4)$$

$$V = \frac{1}{2} \sum_{i \neq j} v(r_i - r_j), \quad (5)$$

where r_n is a combined index for the position and spin of an electron, i.e. $r_n \equiv (\mathbf{r}_n, \sigma_n)$, and assume that $v(r_i - r_j)$ is a spin-independent two-body Coulomb interaction.

In second quantization, this Hamiltonian reads

$$\mathcal{H} = \sum_{ij} t_{ij} c_{i\sigma}^\dagger c_{j\sigma} + \hat{V}, \quad (6)$$

where i and j are indices of an orthonormal single-particle basis $\{\phi_{i\sigma}\}$, and σ denotes the spin. For convenience, we assume that $\phi_{i\sigma}$ has non-zero elements only in the spin sector σ . The Coulomb interaction has the form

$$\hat{V} = \frac{1}{2} \sum_{ijkl} \sum_{\sigma_1 \sigma_2 \sigma_3 \sigma_4} V_{ijkl}^{\sigma_1 \sigma_2 \sigma_3 \sigma_4} c_{i\sigma_1}^\dagger c_{j\sigma_2}^\dagger c_{k\sigma_3} c_{l\sigma_4}, \quad (7)$$

with

$$V_{ijkl}^{\sigma_1 \sigma_2 \sigma_3 \sigma_4} = \int d\mathbf{r} d\mathbf{r}' \phi_{i\sigma_1}^*(\mathbf{r}) \phi_{j\sigma_2}^*(\mathbf{r}') v(\mathbf{r} - \mathbf{r}') \times \phi_{k\sigma_3}(\mathbf{r}') \phi_{l\sigma_4}(\mathbf{r}) \quad (8)$$

and $c_{i\sigma}$ and $c_{i\sigma}^\dagger$ the annihilation and creation operators for the single-particle basis, respectively. In practice, we only consider density-density terms. For example, the onsite repulsion U_α and the inter-orbital interaction U' are represented by

$$U_\alpha = \int d\mathbf{r} d\mathbf{r}' \phi_{i\alpha}^2(\mathbf{r}) V(\mathbf{r}, \mathbf{r}') \phi_{i\alpha}^2(\mathbf{r}'), \quad (9)$$

$$U' = \int d\mathbf{r} d\mathbf{r}' \phi_{i\alpha}^2(\mathbf{r}) V(\mathbf{r}, \mathbf{r}') \phi_{i\beta}^2(\mathbf{r}'). \quad (10)$$

Now, let us consider a non-interacting band structure in which only a few bands are crossing the Fermi level and these low-energy target bands are sandwiched by high-energy screening bands. Figure 3 illustrates a simple example, which has one target band and two screening bands. In the downfolding, we derive an effective model for the target manifold by integrating out the high-energy screening bands. The effective model has the form

$$\mathcal{H} = \sum_{ij} \bar{t}_{ij} d_{i\sigma}^\dagger d_{j\sigma} + \hat{W}, \quad (11)$$

where we introduced a new single-particle basis $\{\bar{\phi}_{i\sigma}\}$ and hopping parameters \bar{t}_{ij} to describe the band structure

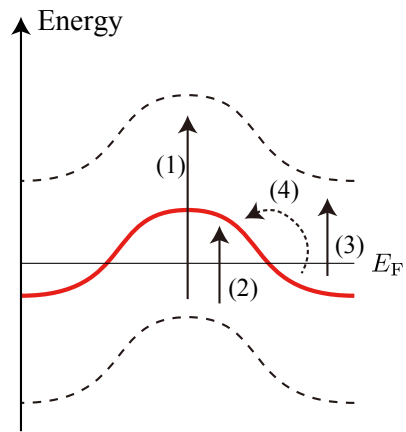


FIG. 3: Schematic band structure. The solid line denotes the low-energy band in the target manifold of the low-energy model, while screening bands are denoted by broken lines. Solid and broken arrows show possible contributions to the polarization: excitations between (1) occupied screening bands and unoccupied screening bands, (2) occupied screening bands and unoccupied target bands, (3) occupied target bands and unoccupied screening bands, (4) occupied target bands and unoccupied target bands. In the cRPA method, we exclude the contribution of (4) because this should be taken into account in solving the low-energy effective model.

in the target manifold. The annihilation and creation operators of $\{\bar{\phi}_{i\sigma}\}$ are given by d and d^\dagger , respectively. We usually take $\bar{\phi}$ to be localized in real space so that the effective interaction is as short-ranged as possible. In first-principles calculations based on a plane-wave basis, the maximally localized Wannier functions^{17,18} are a common choice.

The screened interaction $w(r, r')$ is given by

$$w(r, r') = v(r, r') + \int d\mathbf{r}_1 d\mathbf{r}_2 v(r, \mathbf{r}_1) P(\mathbf{r}_1, \mathbf{r}_2) w(\mathbf{r}_2, r'), \quad (12)$$

where the polarization P is calculated as⁸

$$P(r, r'; \omega) = \sum'_{n,m} f(\epsilon_n) (1 - f(\epsilon_m)) \times \left(\frac{A_{n,m}(r, r')}{\omega - (\epsilon_m - \epsilon_n) + i\delta} - \frac{A_{n,m}^*(r, r')}{\omega + (\epsilon_m - \epsilon_n) - i\delta} \right), \quad (13)$$

with

$$A_{n,m}(r, r') = \Psi_n^*(r) \Psi_n(r') \Psi_m(r) \Psi_m^*(r'). \quad (14)$$

Here, Ψ_n is the n -th eigenstate of H^0 and f is the Fermi function. In Fig. 3, we show possible contributions to the sum in Eq. (13). Since the contribution to the polarization from transitions within the target subspace will be treated more accurately by solving the effective model, the contribution denoted by (4) in Fig. 3 is excluded in the sum in Eq. (13). The symbol \sum' means that these

contributions are excluded. Since P is spin-diagonal and v is spin-independent, Eq. (12) reads

$$\begin{aligned} w(\mathbf{r}\sigma, \mathbf{r}'\sigma') &= v(\mathbf{r}, \mathbf{r}') + \int d\mathbf{r}_1 d\mathbf{r}_2 \sum_{\sigma_1, \sigma_2} v(\mathbf{r}\sigma, \mathbf{r}_1\sigma_1) \delta_{\sigma_1\sigma_2} P(\mathbf{r}_1\sigma_1, \mathbf{r}_2\sigma_2) \\ &\quad \times w(\mathbf{r}_2\sigma_2, \mathbf{r}'\sigma'), \\ &= v(\mathbf{r}, \mathbf{r}') + 2 \int d\mathbf{r}_1 d\mathbf{r}_2 v(\mathbf{r}, \mathbf{r}_1) P(\mathbf{r}_1, \mathbf{r}_2) w(\mathbf{r}_2, \mathbf{r}'). \end{aligned} \quad (15)$$

The factor of 2 in the last line comes from the sum over two screening processes involving different spin sectors of P , i.e., $P(\uparrow, \uparrow)$ and $P(\downarrow, \downarrow)$.

Once the screened two-body interaction has been computed, the screened interaction is projected onto the basis of the target manifold. Replacing $v(\mathbf{r} - \mathbf{r}')$ with $w(\mathbf{r} - \mathbf{r}')$ in Eq. (8), the screened interaction is given by

$$\hat{W} = \frac{1}{2} \sum_{ijkl} \sum_{\sigma_1\sigma_2\sigma_3\sigma_4} W_{ijkl}^{\sigma_1\sigma_2\sigma_3\sigma_4} d_{i\sigma_1}^\dagger d_{j\sigma_2}^\dagger d_{k\sigma_3} d_{l\sigma_4}. \quad (16)$$

Here, $\hat{d}_{i\sigma}$ and $\hat{d}_{i\sigma}^\dagger$ are the annihilation and creation operators corresponding to Wannier orbitals of the target manifold, which will be constructed below. The matrix \mathbf{W} is given by

$$\begin{aligned} W_{ijkl} &= \int d\mathbf{r} d\mathbf{r}' \bar{\phi}_{i\sigma_1}^*(\mathbf{r}) \bar{\phi}_{j\sigma_2}^*(\mathbf{r}') w(\mathbf{r} - \mathbf{r}') \\ &\quad \times \bar{\phi}_{k\sigma_3}(\mathbf{r}') \bar{\phi}_{l\sigma_4}(\mathbf{r}). \end{aligned} \quad (17)$$

The ω dependence of W can be accounted for in the solution of the effective model.

A convenient way to solve the cRPA equation is to introduce the so-called product basis.¹⁹ Assuming that the orthonormal localized basis ϕ_i is real, that is, $\phi_i^*(\mathbf{r}) = \phi_i(\mathbf{r})$, the product basis is defined by

$$\{B_{ij}(\mathbf{r})\} = \{\phi_i(\mathbf{r})\phi_j(\mathbf{r})\}. \quad (18)$$

Note that the product basis is not orthonormal. In the following, we use I and I' to refer to the index of the product basis, that is, $I \equiv (ij)$. We expand $P(r, r')$ in terms of the product basis as

$$\begin{aligned} P(r, r') &= \delta_{\sigma\sigma'} P(\mathbf{r}, \mathbf{r}') \\ &= \delta_{\sigma\sigma'} \sum_{I, I'} P_{II'} B_I(\mathbf{r}) B_{I'}(\mathbf{r}'). \end{aligned} \quad (19)$$

Then, Eq. (15) and (17) lead to

$$\begin{aligned} W_{ijkl} &= W_{II'} \\ &= \int d\mathbf{r} d\mathbf{r}' B_I(\mathbf{r}) W(\mathbf{r} - \mathbf{r}') B_{I'}(\mathbf{r}') \\ &= \int d\mathbf{r} d\mathbf{r}' B_I(\mathbf{r}) V(\mathbf{r} - \mathbf{r}') B_{I'}(\mathbf{r}') \\ &\quad + 2P_{I_1 I_2} \int d\mathbf{r} d\mathbf{r}_1 B_I(\mathbf{r}) V(\mathbf{r} - \mathbf{r}_1) B_{I_1}(\mathbf{r}_1) \\ &\quad \times \int d\mathbf{r}_2 d\mathbf{r}' B_{I_2}(\mathbf{r}_2) W(\mathbf{r}_2 - \mathbf{r}') B_{I'}(\mathbf{r}') \\ &= V_{II'} + 2 \sum_{I_1 I_2} V_{I_1 I_2} P_{I_1 I_2} W_{I_2 I'}, \end{aligned} \quad (20)$$

where we take $I = (ik)$ and $I' = (jl)$. This equation can be written in matrix representation as

$$\mathbf{W} = \mathbf{V} + 2\mathbf{V}\mathbf{P}\mathbf{W} = (\mathbf{I} - 2\mathbf{V}\mathbf{P})^{-1}\mathbf{V}. \quad (21)$$

We do not need to consider the spin degrees of freedom in Eq. (21) since Eq. (15) is already spin-independent.

For our model, the product basis is given by

$$\{B_I\} = \{\phi_{ia}^2\}, \quad (22)$$

since we include only density-density interactions. In other words, the integral in Eq. (8) vanishes whenever terms like $\phi_{ia}(\mathbf{r})\phi_{jb}(\mathbf{r})$ ($i \neq j$ or $a \neq b$) appear. The index a denotes orbital and does not include spin.

We define the Fourier transformations of the bare Coulomb interaction V and the polarization P as

$$V_{ab}(\mathbf{q}) = \frac{1}{N_k} \sum_i U_{ij}^{ab} e^{-i\mathbf{q}\cdot(\mathbf{R}_i - \mathbf{R}_j)} = \frac{1}{N_k} U^{ab}, \quad (23)$$

$$P_{ab}(\mathbf{q}) = \frac{1}{N_k} \sum_i P_{ij}^{ab} e^{-i\mathbf{q}\cdot(\mathbf{R}_i - \mathbf{R}_j)}. \quad (24)$$

Diagonalizing the Fourier transformation of the one-body Hamiltonian, one obtains Bloch wavefunctions:

$$\begin{aligned} \Psi_{ka}(r) &= \frac{1}{\sqrt{N_k}} \sum_i c_{kn,a} \phi_{ia}(r) e^{ikR_i}, \\ &= \frac{1}{\sqrt{N_k}} \sum_i \begin{pmatrix} c_{kn,1} \\ c_{kn,2} \\ \vdots \\ c_{kn,N} \end{pmatrix} e^{ikR_i}, \end{aligned} \quad (25)$$

where n is the band index. Substituting this equation into Eq. (14), and using

$$\begin{aligned} P(r, r'; \omega) &= \sum_{n,m}^I f(\epsilon_n) (1 - f(\epsilon_m)) \times \\ &\quad \left(\frac{A(r, r')}{\omega - (\epsilon_m - \epsilon_n) + i\delta} - \frac{A^*(r, r')}{\omega + (\epsilon_m - \epsilon_n) - i\delta} \right), \end{aligned} \quad (26)$$

we obtain

$$P_{ab}(\mathbf{q}; \omega) = \frac{1}{N_k} \sum_{knn'} f_{k,n} (1 - f_{k+q,n'}) \times \left[\frac{c_{kn}^*(a) c_{k+qn'}(a) c_{kn}(b) c_{k+qn'}^*(b)}{\omega - (\epsilon_{k+q,n'} - \epsilon_{k,n}) + i\delta} - \frac{c_{kn}(a) c_{k+qn'}^*(a) c_{kn}^*(b) c_{k+qn'}(b)}{\omega + (\epsilon_{k+q,n'} - \epsilon_{k,n}) - i\delta} \right], \quad (27)$$

where $\epsilon_{k,n}$ is the n -th eigenvalue at wavevector k .

In reciprocal space, the cRPA equation reads

$$W_{ab}(\mathbf{q}) = V(\mathbf{q})_{ab} + 2 \sum_{cd} V_{ac}(\mathbf{q}) P_{cd}(\mathbf{q}) W_{db}(\mathbf{q}), \quad (28)$$

where a, b, c, d are orbital indices. This can be rewritten in matrix form as

$$\mathbf{W}(\mathbf{q}) = [\mathbf{I} - 2\mathbf{V}(\mathbf{q})\mathbf{P}(\mathbf{q})]^{-1}\mathbf{V}(\mathbf{q}). \quad (29)$$

Next, $\mathbf{W}(\mathbf{q})$ is projected onto a localized basis for the target band(s). A set of Wannier functions localized in the unit cell \mathbf{R}_i is defined by

$$|\mathbf{R}_i n\rangle = \frac{1}{N_k} \sum_{\mathbf{k}} \left(\sum_m \mathcal{U}_{mn}^{\mathbf{k}} e^{-i\mathbf{k}\cdot\mathbf{R}_i} |\Psi_{m\mathbf{k}}\rangle \right) = \sum_j \alpha_{ija}^n \phi_{ja}(\mathbf{r}). \quad (30)$$

where $n = 1, \dots, N_{\text{band}}$ is the index of the Wannier function in a unit cell (N_{band} is the number of target bands). The symbol a denotes the orbital index in the unit cell j . When we construct maximally localized Wannier functions^{17,18} from Bloch wavefunctions obtained by first-principles calculations, the gauge matrix $\mathcal{U}_{mn}^{\mathbf{k}}$ is chosen so that the Wannier functions are localized in real space.

To obtain $\mathcal{U}_{mn}^{\mathbf{k}}$ we write the non-interacting part of the Hamiltonian of our model as

$$\mathbf{H}(\mathbf{k}) = -2(\cos(k_x) + \cos(k_y) + \cos(k_z)) \mathbf{I} + \langle H(\mathbf{k}) \rangle_{\mathbf{k}}, \quad (31)$$

where

$$\langle H(\mathbf{k}) \rangle_{\mathbf{k}} = \begin{pmatrix} 0 & -t' \\ -t' & 0 \end{pmatrix}. \quad (32)$$

Since the Bloch wavefunction is independent of wavevector, we can take a unitary matrix $\mathbf{U} = \{\mathbf{u}_1, \dots, \mathbf{u}_{N_{\text{orb}}}\}$ that diagonalizes $\langle H(\mathbf{k}) \rangle_{\mathbf{k}}$, and denote the eigenvalues by $\epsilon_1, \dots, \epsilon_{N_{\text{orb}}}$. This also diagonalizes the full non-interacting Hamiltonian at the same time, and the eigenvalues are $-2\cos(\mathbf{k}) + \epsilon_1, \dots, -2\cos(\mathbf{k}) + \epsilon_{N_{\text{orb}}}$. Taking the gauge matrix $\mathbf{U}(\mathbf{k}) = \mathbf{I}$, the Wannier function for the target band localized at site i_0 becomes

$$|i; i_0\rangle = \delta_{ii_0} \mathbf{u}_{\text{target}}, \quad (33)$$

where i is the site index.

Next we project the screened interactions onto the Wannier basis of the target band. The matrix elements in Eq. (16) have non-zero values only when ($i = l$ and $j = k$) and ($\sigma_2 = \sigma_3$ and $\sigma_1 = \sigma_4$). From Eq. (16), we obtain

$$\hat{W} = U \sum_i \hat{n}_{i\uparrow} \hat{n}_{i\downarrow} + \frac{1}{2} \sum_{i \neq j} V_{ij} \hat{n}_i \hat{n}_j, \quad (34)$$

where

$$U = \sum_{ab} W(\mathbf{R} = 0)_{ab} |u_{\text{target}}(a)|^2 |u_{\text{target}}(b)|^2, \quad (35)$$

$$V_{ij} = \sum_{ab} W(\mathbf{R}_i - \mathbf{R}_j)_{ab} |u_{\text{target}}(a)|^2 |u_{\text{target}}(b)|^2. \quad (36)$$

Exchange integrals vanish since orbitals ϕ_{ia} are taken to be delta functions in our model.

IV. DYNAMICAL MEAN-FIELD THEORY

We use variants of the dynamical mean-field theory to analyze the full multi-orbital models and the effective one-band models in a consistent way. We use multi-orbital DMFT for the full models. The effective models are solved using the EDMFT framework which can treat off-site interactions within a single-impurity problem.

A. Multi-orbital DMFT

In order to solve the full multi-orbital model, we use DMFT. Its self-consistency loop is given by

$$\Sigma(i\omega_n) = \mathcal{G}(i\omega_n)^{-1} - \mathbf{G}_{\text{imp}}^{-1}(i\omega_n), \quad (37)$$

$$\mathbf{G}_{\text{loc}}(i\omega_n) = \frac{1}{N_k} \sum_{\mathbf{k}} \frac{1}{i\omega_n + \mu - \mathcal{H}_0(\mathbf{k}) - \Sigma(i\omega_n)}, \quad (38)$$

$$\mathcal{G}(i\omega_n)^{-1} = \mathbf{G}_{\text{loc}}^{-1}(i\omega_n) + \Sigma(i\omega_n), \quad (39)$$

where $\mathcal{H}_0(\mathbf{k})$ is the Fourier transform of the one-body part of the Hamiltonian. Σ , \mathbf{G}_{loc} , and \mathcal{G} are the self-energy, local Green's function, and the Weiss function, respectively. Since we consider the paramagnetic case, they are $N_{\text{orb}} \times N_{\text{orb}}$ matrices.

After obtaining \mathcal{G} in Eq. (39), we solve the multi-orbital quantum impurity problem given by the action

$$S = - \sum_{ab\sigma} \int_0^\beta d\tau d\tau' c_{a\sigma}^\dagger(\tau) \mathcal{G}_{ab}^{-1}(\tau - \tau') c_{b\sigma}(\tau') + \frac{1}{2} \sum_{ab} \int_0^\beta d\tau U_{ab} n_a(\tau) n_b(\tau), \quad (40)$$

where U_{ab} is the onsite part of the density-density interaction. We employ continuous-time quantum Monte

Carlo impurity solvers based on the hybridization expansion.^{20,21} The three- and five-orbital models are solved with the matrix formalism²¹ and the Krylov algorithm.²² We furthermore improve the efficiency of the Monte Carlo sampling by the sliding-window update²³ and “lazy trace evaluation”.²⁴ The sign problem is reduced by rotating the basis of the hybridization function. We refer to Appendices A and B for details.

After computing \mathbf{G} , Σ is updated using Eq. (37) and the self-consistent loop is repeated until a converged solution is obtained.

In our analyses, we project the Green’s function $\mathbf{G}(i\omega_n)$ onto the basis that diagonalizes $\langle H(k) \rangle_k$ as

$$G_m(i\omega_n) = \mathbf{u}_m^\dagger \mathbf{G}(i\omega_n) \mathbf{u}_m, \quad (41)$$

where \mathbf{u}_m is the m -th eigenvector of $\langle H(k) \rangle_k$. The Green’s function is defined by

$$\mathbf{G}_{ab}(\tau) = -\langle T_\tau c_a(\tau) c_b^\dagger(0) \rangle, \quad (42)$$

$$\mathbf{G}_{ab}(i\omega_n) = \int_0^\beta d\tau e^{i\omega_n \tau} \mathbf{G}(\tau), \quad (43)$$

where T_τ denotes imaginary-time ordering and $\omega_n = (2n+1)\pi/\beta$. We call this basis the “band basis”. The renormalization factor Z is computed by using the approximation

$$Z = \frac{1}{1 - \frac{\partial \Sigma_m(\omega)}{\partial \omega}} \approx \frac{1}{1 - \frac{\text{Im} \Sigma_m(i\omega_0)}{\pi/\beta}}, \quad (44)$$

where m is the index of the target band.

B. EDMFT

To solve the effective one-band model with dynamical on-site and off-site interactions, we use extended DMFT (EDMFT),^{25–29} This formalism can treat off-site interactions, even though it is based on a single-site impurity construction. In the present study, we consider only dynamical nearest-neighbor interactions. In the EDMFT calculation, we have to solve the impurity problem

$$S = - \sum_{ab\sigma} \int_0^\beta d\tau d\tau' c_{a\sigma}^\dagger(\tau) \mathcal{G}_{ab}^{-1}(\tau - \tau') c_{b\sigma}(\tau') + \int_0^\beta d\tau d\tau' n^\dagger(\tau) U(\tau - \tau') n(\tau'). \quad (45)$$

The retarded interaction $U(\tau)$ is determined by the following self-consistent equations, which are similar to Eqs. (38)–(37):

$$W_{\text{imp}}(i\nu_n) = \mathcal{U}(i\nu_n) - \mathcal{U}(i\nu_n) \chi_{\text{imp}}(i\nu_n) \mathcal{U}(i\nu_n), \quad (46)$$

$$\Pi(i\nu_n) = U(i\nu_n)^{-1} - W_{\text{imp}}^{-1}(i\nu_n), \quad (47)$$

$$W_{\text{loc}}(i\nu_n) = \frac{1}{N_k} \sum_k \frac{1}{v_k^{-1}(i\nu_n) - \Pi(i\nu_n)}, \quad (48)$$

$$U(i\nu_n)^{-1} = W_{\text{loc}}^{-1}(i\nu_n) + \Pi(i\nu_n), \quad (49)$$

where

$$v_k(i\nu_n) = \sum_i v_i(i\nu) e^{i r_i k}, \quad (50)$$

$$\chi_{\text{imp}}(\tau) = \langle n(\tau) n(0) \rangle - \langle n \rangle^2. \quad (51)$$

This impurity problem with retarded density-density interaction is also solved by the hybridization expansion method.^{20,21,30,31}

V. RESULTS

A. Downfolded models

We now derive low-energy effective models for the three-orbital and five-orbital models using the cRPA method. We start with the three-orbital case. Figures 4(a) and 4(b) show the onsite interaction $U(\omega)$ and nearest-neighbor interaction $V_{\text{nn}}(\omega)$ computed for $t' = 2$ and $\Delta = 7$. For all the parameters considered ($U'/U_d = 0.4$ and 0.5 , $U_d = 10$ and 20) $\text{Im}U(\omega)$ exhibits a negative peak around the energy scale set by transitions between the lowest band and the highest band, i.e., $\omega_{\text{ex}} = 2\Delta = 14$. Below ω_{ex} , the onsite interaction is reduced compared to the instantaneous value $U(\omega = \infty)$. Note that $U(\omega = \infty)$ is smaller than U_d because the Wannier function extends to the less correlated screening orbitals. Although the full model has only onsite interactions, a dynamic nearest-neighbor interaction $\text{Re}V_{\text{nn}}(\omega)$ is generated around ω_{ex} , as clearly seen in Fig. 4(b). We take into account the nearest-neighbor interactions in the following EDMFT analyses. However, because the nearest-neighbor interaction almost vanishes at low frequencies, the dynamic off-site interactions can be expected to play a minor role in determining the low-temperature properties of the present model.

To quantify the strength of the screening of the onsite interaction, we evaluate

$$\Lambda \equiv 1 - \frac{\text{Re}U(\omega = 0)}{\text{Re}U(\omega = \infty)}, \quad (52)$$

for different U' and U_d . The result is shown in Fig. 5(a) as a function of U_d . Two notable trends are discernible. First, Λ becomes larger in the strongly correlated regime, that is, as U_d increases. Second, Λ increases if U'/U_d decreases. This is presumably because reducing U' enhances orbital fluctuations. In the next subsection, we perform DMFT analyses for $U'/U_d = 0.4$ and 0.5 by varying U' .

Next we move on to the five-orbital model. Figure 5(b) shows the U_d dependence of Λ computed for $\Delta = 10$ and $t' = 4$. Despite the increase in Δ , the screening effect is comparable with that of the three-orbital model. One can clearly see the same trends as for the three-orbital model: Increasing U_d and decreasing U'/U_d enhances the screening effect. The dependence on t' is shown in Fig. 5(c). The screening effect is maximally enhanced around $t' \simeq 4$.

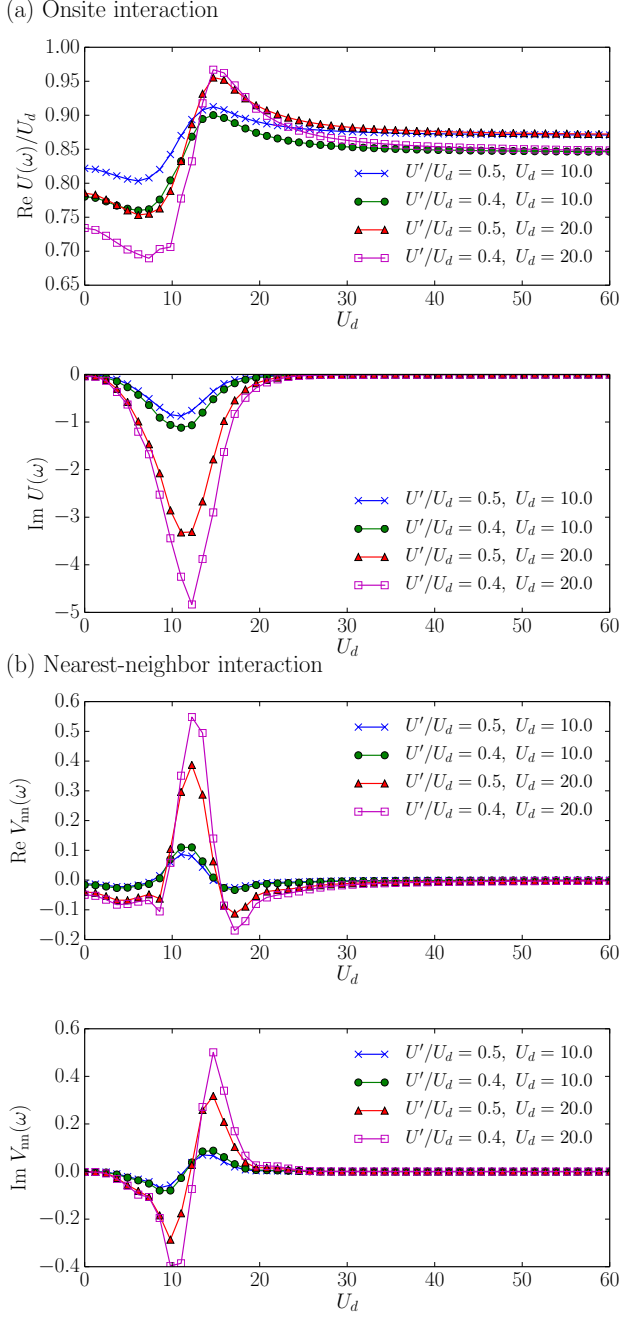


FIG. 4: (Color online) Dynamically screened onsite interaction $U(\omega)$ and nearest neighbor interaction $V_{nn}(\omega)$ obtained by cRPA for the three-orbital model ($\Delta = 7$ and $t' = 2$).

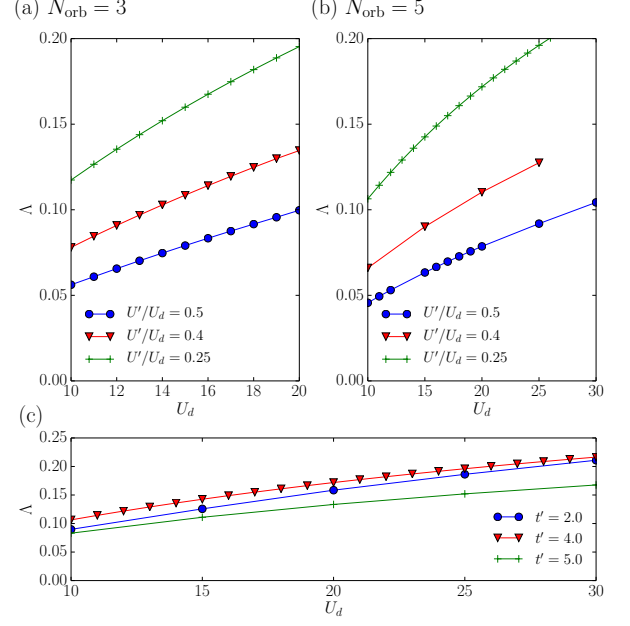


FIG. 5: (Color online) Strength of the screening effect for the onsite interaction Λ for (a) the three-orbital model ($\Delta = 7$ and $t' = 2$) and (b) the five-orbital model ($\Delta = 10$ and $t' = 4$). The definition of Λ is given in Eq. (52). (c) t' dependence of Λ for the five-orbital model ($\Delta = 10$ and $U'/U_d = 0.25$).

B. DMFT results: three-orbital model

We start by analyzing the three-orbital model and the downfolded model within the DMFT or EDMFT framework. In particular, we compare DMFT solutions of the following models: (i) the downfolded single-band model, (ii) the single-band model with the bare interaction [$U(\omega) = U(\omega = \infty)$, $V_{nn}(\omega) = V_{nn}(\omega = \infty)$], and (iii) the full model. In the following, we will refer to these models as the *downfolded model*, the *unscreened model*, and the *full model*, respectively. The simulations are carried out at $\beta = 15$ unless otherwise stated. We confirmed that the temperature is low enough to see ground-state behavior.

First, we investigate the metal-insulator transition by changing U_d for fixed U'/U_d . Figures 6(a) and 6(b) show the local Green's function computed by solving the full model for $U'/U_d = 0.5$ and 0.4 . We start with the results for $U'/U_d = 0.5$ in Fig. 6(a). As U_d increases, the Green's function becomes insulating at $U_d \simeq 15$, signaling a Mott transition. Figure 7(a) compares the local Green's functions computed for the three models. At $U_d = 10$, the screening effects are small, and the three models give metallic Green's functions, whose frequency dependences are consistent. As we increase U_d , the effects of the cRPA screening become clear: At $U_d = 14$, the unscreened model already shows insulating behavior, while the downfolded and the full model remain

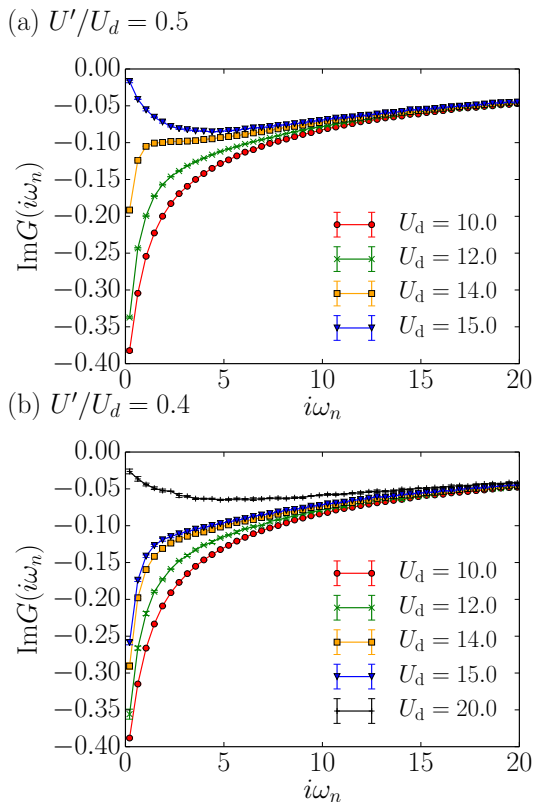


FIG. 6: (Color online) Local Green's function computed for the three-orbital model with $\Delta = 7$ and $t' = 2$ ($\beta = 15$). We project the local Green's function on the target band following Eq. (41).

metallic. The downfolded model quantitatively reproduces the frequency dependence of the local Green's function. As shown in Fig. 6(b), we also see a similar trend for $U_d = 0.4$. A notable difference is that $\text{Im}G(i\omega_n)$ does not vanish at low frequencies even at large U_d , i.e., $\text{Im}G(i\omega_n \rightarrow 0) \neq 0$, which indicates bad metallic behavior. As we will see in the analysis of the spectral function, in this regime, the upper screening band is pulled down by the Coulomb interactions and gets too close to the Fermi level. A similar trend of stabilization of a metallic phase by reducing an inter-orbital Coulomb interaction has been observed for a three-orbital Emery dp model.³²

To make a more quantitative comparison, we show the quasi-particle weights of the three models in Fig. 8. In Fig. 8(a), we clearly see that for $U'/U_d = 0.5$ the downfolded model reproduces the quasi-particle weights rather well up to the Mott transition. For $U'/U_d = 0.4$, the quasi-particle weight of the full model exhibits a tail and does not vanish linearly with increasing U_d , a behavior consistent with the bad metallic behavior seen in $\text{Im}G(i\omega_n)$. Another notable point is that the quasi-particle weights are *overestimated* by the downfolded model in the weakly correlated regime for both $U_d = 0.5$ and 0.4 , although the differences are small. This trend is contrary to the naive expectation that cRPA describes

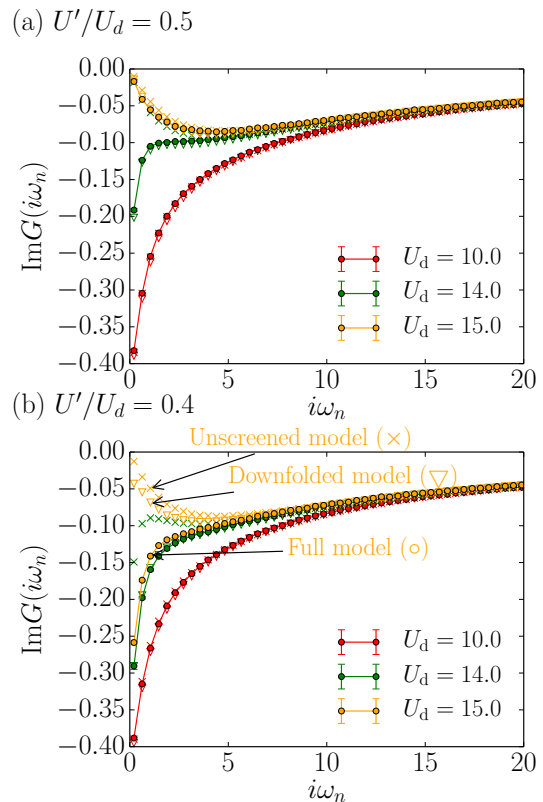


FIG. 7: (Color online) Comparison of the local Green's function for the three-orbital model with $\Delta = 7$ and $t' = 2$ ($\beta = 15$). The circles, triangles, and crosses denote the data obtained by solving the full model, the downfolded model and the unscreend model, respectively.

the screening effects correctly in the weakly correlated regime.

To get some insights into these aspects (the bad metallic behavior and the slight inconsistency in the weakly correlated regime), we compute the spectral function using the maximum-entropy analytic continuation method.³³ The results are shown in Fig. 9 for typical parameters. First, we discuss the data for $U'/U_d = 0.5$. As U_d increases, the lower screening band shifts to lower and lower energies. At the same time, the upper screening band is approaching the Fermi level, although less rapidly. This U_d dependence can be understood by considering single-particle excitations in the atomic limit, i.e., for $t' = 0$ and $t = 0$. In the ground state, the three orbitals are filled, half filled, and empty, respectively [see illustration in Fig. 10(a)]. First, we remove a spin from the lowest orbital [see Fig. 10(b)]. This excitation costs

$$\Delta E_{\text{hole}} = -U_r - U' + \mu + \Delta = U' + \Delta, \quad (53)$$

where μ ($= U_d/2 + 2U'$) is the chemical potential and U_r ($= U_d/2$) is the onsite Coulomb interaction on the screening orbitals. On the other hand, putting an electron into the highest orbital results in the excited state

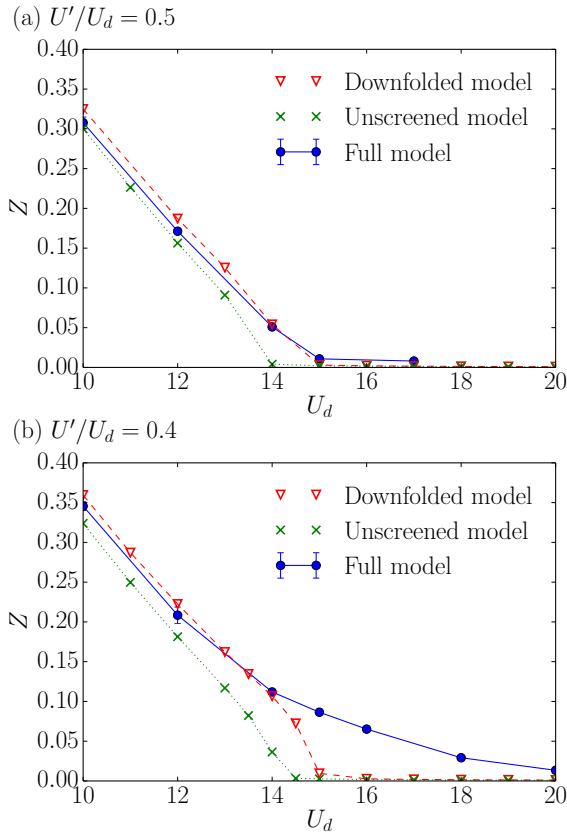


FIG. 8: (Color online) Quasi-particle weights computed for the three-orbital model with $\Delta = 7$ and $t' = 2$. We compare the results of the downfolded model, the unscreened model, and the full model.

shown in Fig. 10(c). The excitation energy is given by

$$\Delta E_{\text{electron}} = 3U' - \mu + \Delta = U' - \frac{U_d}{2} + \Delta. \quad (54)$$

ΔE_{hole} and $\Delta E_{\text{electron}}$ correspond to the positions of the lower and upper screening bands in the spectral function, respectively. When we increase U_d with U'/U_d fixed, ΔE_{hole} increases linearly with U_d . On the electron side, $\Delta E_{\text{electron}}$ stays constant for $U' = U_d/2$ or decreases for $U' < U_d/2$ as U_d increases. This explains the observed shifts in the spectral function.

To see how the shift of the low-lying screening band modifies the effective interactions, we compute the on-site interaction $U(\omega)$ within cRPA by changing the position of the lower screening band. We take $U'/U_d = 0.5$, $U_d = 10$ and keep the other parameters fixed. The result is shown in Fig. 11. As we push down the screening band, the instantaneous value $U(\omega = \infty)$ increases, because the Wannier function becomes more localized on the target orbital. At the same time, Λ becomes smaller because the polarization between the bands becomes smaller. As a combination of these effects, at $\Delta E = 5$, $U(\omega = 0)$ is

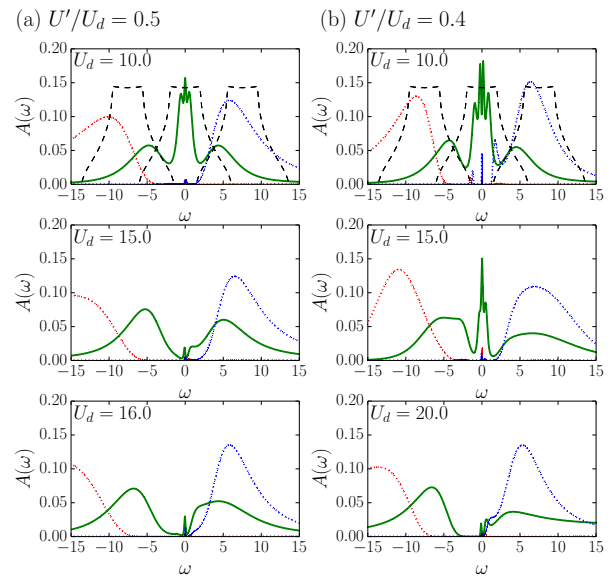


FIG. 9: (Color online) Spectral functions projected on the band basis. The data were obtained by solving the three-orbital model with $\Delta = 7$ and $t' = 2$ at $\beta = 15$. The data for the target band are shown by the solid lines. The dashed lines in the upper panels show the non-interacting density of states.

about 10 % larger than the original value, which can explain the overestimation of the screening effect by cRPA.

We summarize our results in a phase diagram shown in Fig. 12. For the full model, the critical point of the Mott transition is determined by the low-frequency data of the local Green's function: The insulating phase is identified by the criterion that $\text{Im}G(i\omega_0) > \text{Im}G(i\omega_1)$. We also indicate the region where the downfolded and unscreened models qualitatively reproduce the local Green's function in the metallic phase. The boundary is determined by the deviation between the Green's functions of the full and effective models at low frequencies. In particular, we plot lines corresponding to $r = 0.1$, where r is the relative deviation defined by

$$r = \frac{1}{N} \sum_{n=0}^{n < N} |\text{Im}\Delta G(i\omega_n)| \quad (55)$$

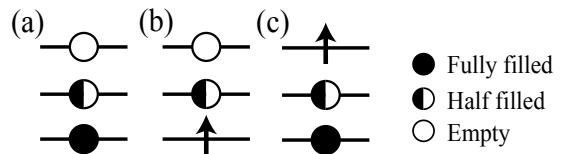


FIG. 10: Single-particle excitations in the atomic limit: (a) the ground state, (b) the excited state with an additional hole in the lowest orbital, and (c) the excited state with an additional spin in the highest orbital. We assume that half-filled target orbitals are paramagnetic.

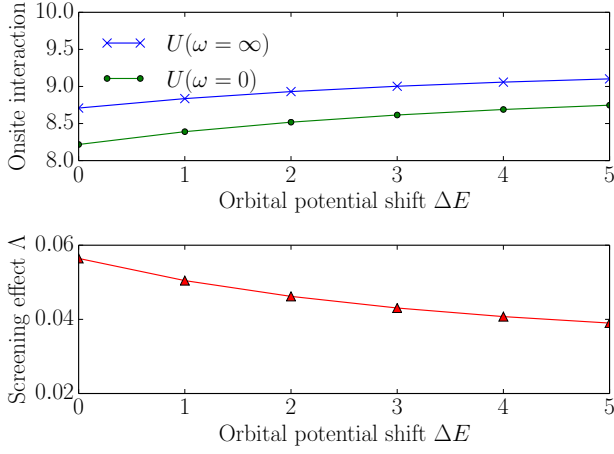


FIG. 11: (Color online) Dependence of screening effects on the position of the lowest band for $U'/U_d = 0.5$, $t' = 2$ and $U_d = 10$. The lowest band is shifted down in energy by ΔE with $0 \leq \Delta E \leq 5$.

with $N = 20$ and $\Delta G(i\omega_n)$ the error of the local Green's function at frequency $i\omega_n$. At $U'/U_d = 0.5$, the downfolded model reproduces the metallic solution well up to the critical value, while the unscreened model fails near the Mott transition. With decreasing U'/U_d , the critical value of the transition shifts toward larger U_d . At the same time, the downfolded model starts to fail near the Mott transition. In the region where the downfolded model fails, the full model shows a bad metallic behavior

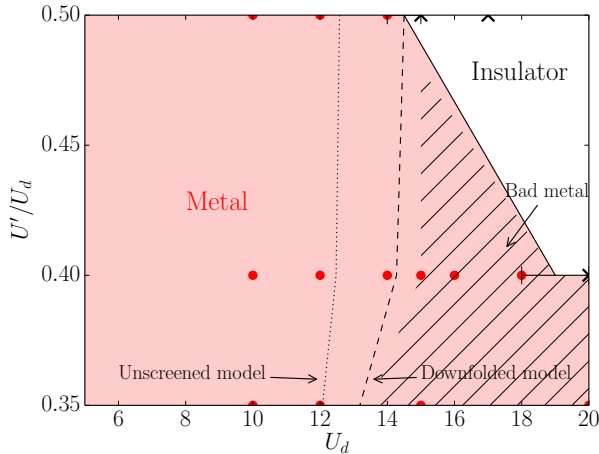


FIG. 12: (Color online) Phase diagram of the three-orbital model for $\Delta = 7$ and $t' = 2$ at $\beta = 15$. The solid line denotes the Mott transition. The dashed and dotted lines represent the upper limits of the regions where the downfolded and unscreened models reproduce the local Green's function, respectively. See the text for more details. The hashed region indicates the parameter space where the bad metallic behavior is seen.

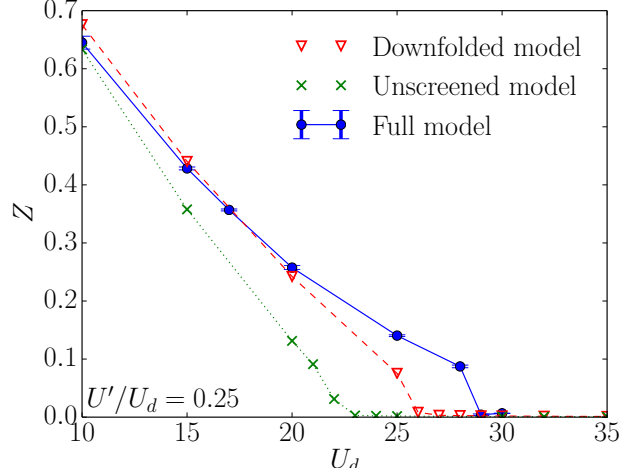


FIG. 13: (Color online) Quasi-particle weights of the five-orbital model for $\Delta = 10$ and $t' = 4$ at $\beta = 15$. We compare the results of the downfolded model, the unscreened model, and the full model.

because the upper screening band gets close to or even touches the Fermi level (see Figs. 8 and 9). Furthermore, the state of the full model is clearly particle-hole asymmetric, while the downfolded model is symmetric by construction (neglecting the small off-site interactions). Obviously, it is impossible to reproduce these multi-orbital effects in the downfolded single band system. However, apart from this hashed region close to the the Mott transition, the downfolded model provides a correct description of the Green's function of the target band in the metallic phase.

C. DMFT results: five-orbital model

A larger number of screening bands in the full model enhances the screening effects. With more bands, we can thus take a larger Δ in order to prevent the bad metallic behavior at small U'/U_d . In the following, we use $\Delta = 10$, $t' = 4$. Figure 13 shows the quasi-particle weights computed for the full, downfolded, and screened models at $U'/U_d = 0.25$ ($\beta = 15$). The full model exhibits a Mott transition between $U_d = 28$ and 29 , while the downfolded model slightly underestimates the critical value as $25 < U_d < 26$. The quasi-particle weights are substantially underestimated near the transition point. Figure 14 shows the local Green's function. Consistent with the results for the quasi-particle weight, the downfolded model reproduces the Green's function up to $U_d = 20$, but fails close to the Mott transition point.

Similar to the three-orbital case, the quasi-particle weights are overestimated by the downfolded model in the weakly correlated regime ($U_d \leq 15$). Figure 15 plots the spectral function. One can see a shift of the screening bands similar to the three-orbital model: The

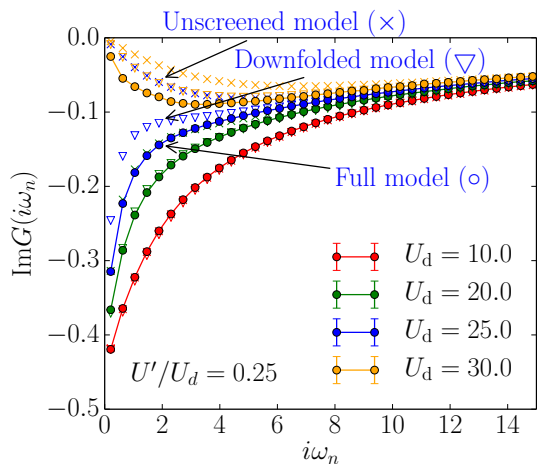


FIG. 14: (Color online) Comparison of the local Green's function computed for the five-orbital model with $\Delta = 10$ and $t' = 4$ ($\beta = 15$). The circles, triangles and crosses denote the data obtained by solving the full model, the downfolded model and the unscreened model, respectively.

lower screening bands are pushed down, while the upper screening bands are pulled down a bit less rapidly by the Coulomb interaction. At $U_d = 10$, the lower edges of the upper screening bands stay at almost the same position. This trend can be explained by a classical argument similarly to the three-orbital case.

To see how sensitively these band shifts modify the effective interactions near the transition point, we compute $U(\omega)$ by pushing/pulling down the lower/upper screening bands. In particular, we lower (E_1, E_2) and (E_4, E_5), respectively. Figure 16 shows the results obtained for $U_d = 20$. We can see that the effective interaction sensitively changes with the band shift. In particular, the instantaneous value $U(\omega = \infty)$ substantially changes, which is likely due to the localization or delocalization of the Wannier function. This effect dominates over the change in polarization, which appears in Λ (see Fig. 16), and it is expected to be particularly important when Δ is comparable to the inter-orbital hopping t' .

VI. CONCLUSION AND DISCUSSION

By comparing the local Green's function for the three-orbital model and the downfolded model, we have found that cRPA fails in the parameter region where the intra-orbital repulsion U' is small and bad metallic behavior originating from multi-orbital physics appears. Outside of this region, the downfolded model correctly reproduces the metallic solution up to the critical value for the Mott transition. We have also analyzed a five-orbital model with larger energy separations (Δ) between the target band and the screening bands. Here, a good agreement between the full model and the downfolded model was found except that the critical value of the Mott tran-

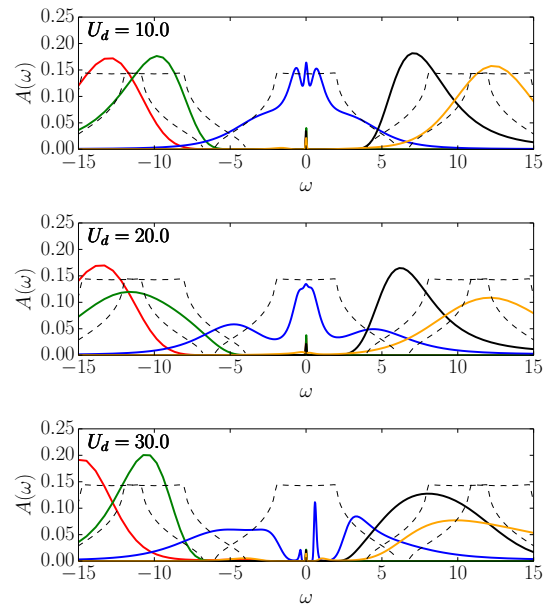


FIG. 15: (Color online) Spectral functions of the five-orbital model for $U'/U_d = 0.25$, $U_d = 10$, $\Delta = 10$ and $t' = 4$ at $\beta = 15$. The dashed lines denote the non-interacting density of states.

sition is underestimated by the downfolded model, and hence the quasi-particle weights are underestimated by the downfolded model near the transition point.

We have furthermore revealed that the quasi-particle weights are *overestimated* by the downfolded model in the weakly correlated metallic regime for both the three-orbital and five-orbital models. By estimating the effective interaction with modified positions of a screening band within cRPA, we have shown that this overestimation can be attributed to the shift of the screening bands by the Coulomb interactions. In particular, we have shown that the Wannier function changes when we shift the screening bands in energy, leading to substantial modifications of the effective interaction.

These observations demonstrate that for a consistent

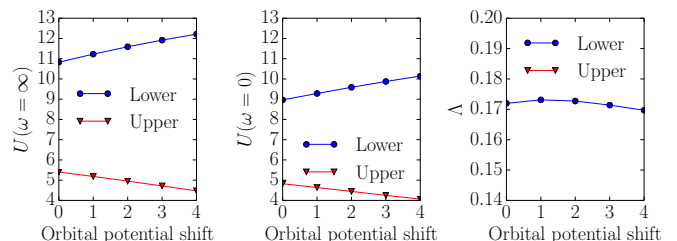


FIG. 16: (Color online) Effective onsite interaction with modified gap sizes of the five-orbital model: $U'/U_d = 0.25$, $U_d = 20$, $\Delta = 10$ and $t' = 4$. We shift (lower) the orbital potentials E_1 and E_2 (Lower) and E_4 and E_5 (Upper), respectively.

description of screening effects in solids, the polarization function should be calculated from interacting propagators. If we compute the polarization function based on the LDA band structure, as is done in the usual cRPA calculations, the correlation effects are only partially taken into account. The modifications of this band structure can be significant when the Coulomb interactions (intra- and inter-orbital repulsions) are comparable to the energy separation between the screening and target manifold. Furthermore, the change in the band structure can also modify the Wannier functions. This effect may play a substantial role when intra-orbital hoppings are comparable to the energy separation between the screening and target manifold. Schemes such as the GW method³⁴ capture at least some of the correlation-induced shifts and renormalizations of the screening bands. In combination with an (E)DMFT treatment of the low-energy bands, an accurate description of strongly correlated materials may be possible, provided that the screened interaction is computed self-consistently, including the feed-back of the DMFT self-energy on the screening bands. Our re-

sults indicate that downfolding based on cRPA may not produce a correct low-energy description of real materials when the band structures used in the calculation of the polarization function overestimate or underestimate the gaps between target and screening bands. It should in general be possible to check whether this criterion is satisfied, e.g., by comparing LDA band structures and (inverse) photoemission spectra.

Acknowledgments

We thank Fakhre Assaad, Ferdi Aryasetiawan, Masatoshi Imada and Shiro Sakai for stimulating discussions and useful comments. We acknowledge support from the DFG via FOR 1346, the SNF Grant 200021E-149122 and ERC Advanced Grant SIMCOFE. The calculations have been performed on the Mönch and Brutus clusters of ETH Zürich using codes based on ALPS.³⁵

-
- ¹ P. Hohenberg and W. Kohn, *Phys.Rev.* **136**, B864 (1964).
² W. Kohn and L. J. Sham, *Physical Review* **140**, A1133 (1965).
³ E. Gull, A. J. Millis, A. I. Lichtenstein, A. N. Rubtsov, M. Troyer, and P. Werner, *Reviews of Modern Physics* **83**, 349 (2011).
⁴ A. Georges, G. Kotliar, W. Krauth, and M. J. Rozenberg, *Reviews of Modern Physics* **68**, 13 (1996).
⁵ D. Ceperley, G. V. Chester, and M. H. Kalos, *Phys.Rev.* **B16**, 3081 (1977).
⁶ U. Schollwöck, *Annals of Physics* **326**, 96 (2011).
⁷ M. Imada and T. Miyake, *Journal of the Physical Society of Japan* **79**, 112001 (2010).
⁸ F. Aryasetiawan, M. Imada, A. Georges, G. Kotliar, S. Biermann, and A. I. Lichtenstein, *Physical Review B* **70**, 195104 (2004).
⁹ K. Nakamura, Y. Yoshimoto, Y. Nohara, and M. Imada, *Journal of the Physical Society of Japan* **79**, 123708 (2010).
¹⁰ T. Miyake, K. Nakamura, R. Arita, and M. Imada, *Journal of the Physical Society of Japan* **79**, 044705 (2010).
¹¹ K. Nakamura, R. Arita, and M. Imada, *Journal of the Physical Society of Japan* **77**, 093711 (2008).
¹² T. Misawa, K. Nakamura, and M. Imada, *Physical Review Letters* **108**, 177007 (2012).
¹³ K. Nakamura, Y. Yoshimoto, T. Kosugi, R. Arita, and M. Imada, *Journal of the Physical Society of Japan* **78**, 083710 (2009).
¹⁴ K. Nakamura, Y. Yoshimoto, and M. Imada, *Physical Review B* **86**, 205117 (2012).
¹⁵ H. Shinaoka, T. Misawa, K. Nakamura, and M. Imada, *Journal of the Physical Society of Japan* **81**, 034701 (2012).
¹⁶ T. Koretsune and C. Hotta, *Physical Review B* **89**, 045102 (2014).
¹⁷ I. Souza, N. Marzari, and D. Vanderbilt, *Physical Review B* **65**, 035109 (2001).
¹⁸ N. Marzari and D. Vanderbilt, *Physical Review B* **56**, 12847 (1997).
¹⁹ F. Aryasetiawan and O. Gunnarsson, *Physical Review B* **49**, 16214 (1994).
²⁰ P. Werner, A. Comanac, L. de' Medici, M. Troyer, and A. Millis, *Physical Review Letters* **97**, 076405 (2006).
²¹ P. Werner and A. Millis, *Physical Review B* **74**, 155107 (2006).
²² A. M. Läuchli and P. Werner, *Physical Review B* **80**, 235117 (2009).
²³ H. Shinaoka, M. Dolfi, M. Troyer, and P. Werner, *Journal of Statistical Mechanics: Theory and Experiment* **2014**, P06012 (2014).
²⁴ P. Sémon, C.-H. Yee, K. Haule, and A. M. S. Tremblay, *Physical Review B* **90**, 075149 (2014).
²⁵ T. Ayril, S. Biermann, and P. Werner, *Physical Review B* **87**, 125149 (2013).
²⁶ Q. Si and J. L. Smith, *Physical Review Letters* **77**, 3391 (1996).
²⁷ A. M. Sengupta and A. Georges, *Physical Review B* **52**, 10295 (1995).
²⁸ P. Sun and G. Kotliar, *Physical Review B* **66**, 085120 (2002).
²⁹ P. Sun and G. Kotliar, *Physical Review Letters* **92**, 196402 (2004).
³⁰ P. Werner and A. Millis, *Physical Review Letters* **99**, 146404 (2007).
³¹ P. Werner and A. J. Millis, *Physical Review Letters* **104**, 146401 (2010).
³² P. Hansmann, N. Parragh, A. Toschi, G. Sangiovanni, and K. Held, *New Journal of Physics* **16**, 033009 (2014).
³³ M. Jarrell and J. E. Gubernatis, *Physics Reports* **269**, 133 (1996).
³⁴ L. Hedin, *Physical Review* **139**, A796 (1965).
³⁵ B. Bauer, L. D. Carr, H. G. Evertz, A. Feiguin, J. Freire, S. Fuchs, L. Gamper, J. Gukelberger, E. Gull, and S. Guertler, *Journal of Statistical Mechanics: Theory and Experiment* **2011**, P05001 (2011).

Appendix A: Details of the multi-orbital DMFT calculations

In this appendix, we describe the detailed procedure of the multi-orbital DMFT calculations in the present study.

Our impurity solver works with the imaginary time hybridization function $\Delta(\tau)$ rather than $\Delta(i\omega_n)$. Since $\mathcal{G}(i\omega_n)$ is computed in frequency space, we have to Fourier transform $\Delta(i\omega_n)$ to imaginary time. To perform this Fourier transformation, we make use of the high-frequency expansion of $\Delta(i\omega_n)$:

$$\Delta(i\omega_n) = \frac{c_1}{i\omega_n} + \frac{c_2}{(i\omega_n)^2} + O(1/(i\omega_n)^3), \quad (\text{A1})$$

where

$$c_1 = -(H_2 - H_1^2), \quad (\text{A2})$$

$$c_2 = H_1^3 - 2H_1H_2 + H_3, \quad (\text{A3})$$

$$H_n \equiv \langle H(k)^n \rangle_k. \quad (\text{A4})$$

The second term gives the lowest expansion coefficient of $\text{Re}\Delta(i\omega_n)$. Since our model does not have particle-hole symmetry, $\text{Re}\Delta(i\omega_n)$ can have a substantial contribution even at high frequencies, where we introduce a cutoff for the Fourier transformation.

To avoid systematic errors due to this cutoff in frequency, we first subtract the contribution of the first two leading terms in Eq. (A1) from $\Delta(i\omega_n)$. Then, we perform a Fourier transformation on the remaining part of $\Delta(i\omega_n)$. We finally add the contribution of the high-frequency expansion

$$-\frac{c_1}{2} + \frac{c_2}{4}(2\tau - \beta) \quad (\text{A5})$$

to $\Delta(\tau)$.

Appendix B: Rotating the single-particle basis when solving a multi-orbital impurity problem

We consider a multi-orbital quantum impurity problem given by the action

$$S = S_{\text{imp}} + \sum_{ab} \int_0^\beta d\tau d\tau' \Delta_{ab}(\tau - \tau') c_a^\dagger(\tau) c_b(\tau'), \quad (\text{B1})$$

where Δ is the hybridization function, which satisfies $\Delta_{ab}(\tau) = \Delta_{ba}^*(\tau)$. S_{imp} is the local impurity action.

One expands the partition function Z as

$$\begin{aligned} Z &= \text{Tr} [e^{-\beta\mathcal{H}}] \\ &= Z_{\text{bath}} \sum_{n=0}^{\infty} \int_0^\beta d\tau_1 d\tau'_1 \cdots \int_0^\beta d\tau_n d\tau'_n \\ &\quad \text{Tr}_{\text{loc}} \left[e^{-\beta\mathcal{H}_{\text{loc}}} T c_{\alpha_n}(\tau_n) c_{\alpha'_n}^\dagger(\tau'_n) \cdots c_{\alpha_1}(\tau_1) c_{\alpha'_1}^\dagger(\tau'_1) \right] \\ &\quad \times \det \mathbf{M}^{-1}, \end{aligned} \quad (\text{B2})$$

where H is the Hamiltonian of the whole system including the impurity and the bath. \mathcal{H}_{loc} is the local Hamiltonian corresponding to S_{imp} . The matrix element of \mathbf{M}^{-1} at (i, j) is given by the hybridization function $\Delta_{\alpha'_i, \alpha_j}(\tau'_i - \tau_j)$. In the Krylov method, we evaluate the trace over the local degrees freedom $\text{Tr}_{\text{loc}}[\cdots]$ by calculating imaginary time evolutions in the occupation number basis.²²

When Δ has non-vanishing off-diagonal elements Δ_{ab} ($a \neq b$), the Monte Carlo sampling according to Eq. (B2) suffers from a negative sign problem. To reduce this sign problem, we rewrite the action Eq. (B1) as

$$S = S_{\text{imp}} + \sum_{ab} \int_0^\beta d\tau d\tau' \bar{\Delta}(\tau - \tau') d_a^\dagger(\tau) d_b(\tau'), \quad (\text{B3})$$

where

$$c_a(\tau) = \sum_b U_{ab} d_b(\tau), \quad (\text{B4})$$

$$c_a^\dagger(\tau) = \sum_b (U^\dagger)_{ab} d_b(\tau), \quad (\text{B5})$$

$$\bar{\Delta}_{ab}(\tau) = \sum_{cd} (U^\dagger)_{ac} \Delta_{cd}(\tau - \tau') U_{db}, \quad (\text{B6})$$

and U_{ab} is a unitary matrix. We choose the unitary matrix U such that the off-diagonal elements of $\bar{\Delta}$ become smaller. In the present study, we choose the single-particle basis that diagonalizes the non-interacting part of \mathcal{H}_{imp} because this diagonalizes the hybridization function at all τ in the non-interacting limit, i.e, $U_d = U' = 0$.

The partition function is then expanded in terms of this new basis as

$$\begin{aligned} Z &= Z_{\text{bath}} \sum_{n=0}^{\infty} \int_0^\beta d\tau_1 d\tau'_1 \cdots \int_0^\beta d\tau_n d\tau'_n \\ &\quad \text{Tr}_{\text{loc}} \left[e^{-\beta\mathcal{H}_{\text{loc}}} T d_{\alpha_n}(\tau_n) d_{\alpha'_n}^\dagger(\tau'_n) \cdots d_{\alpha_1}(\tau_1) d_{\alpha'_1}^\dagger(\tau'_1) \right] \\ &\quad \times \det \bar{\mathbf{M}}^{-1}, \end{aligned} \quad (\text{B7})$$

where the matrix element of $\bar{\mathbf{M}}^{-1}$ is now given by the rotated hybridization function $\bar{\Delta}$. The local trace can be efficiently evaluated in the occupation number basis.